fluids

MDPI

Article

Turbulent Characteristics and Air Entrainment Patterns in Breaking Surge Waves

Zhuoran Li [1], Akash Venkateshwaran [2] and Shooka Karimpour [1,*]

[1] Department of Civil Engineering, Lassonde School of Engineering, York University, Toronto, ON M3J 1P3, Canada; zli29@my.yorku.ca
[2] Department of Mechanical Engineering, Vellore Institute of Technology, Chennai 600127, India; akash.v2018@vitstudent.ac.in
* Correspondence: shooka.karimpour@lassonde.yorku.ca

Abstract: Breaking surge waves are highly turbulent three-dimensional (3D) flows, which occur when the water flow encounters a sudden change in depth or velocity. The 3D turbulent structures across a breaking surge are induced by the velocity gradient across the surge and phase discontinuity at the front. This paper examined the turbulent structures in breaking surge waves with Froude numbers of 1.71 and 2.13 by investigating the air entrainment and perturbation patterns across the surge front. A combination of the Volume Of Fluid (VOF) method and Large Eddy Simulation (LES) was utilized to capture air entrainment and turbulent structures simultaneously. The 3D nature of the vortical structures was simulated by implementing a spanwise periodic boundary. The water surface perturbation and air concentration profiles were extracted, and the averaged air concentration profiles obtained from the numerical simulations were consistent with laboratory observations reported in the literature. The linkage between turbulent kinetic energy distribution and air entrainment was also explored in this paper. Finally, using quadrant analysis and the *Q*-criterion, this paper examined the role of the spanwise perturbations in the development of turbulent structures in the surge front.

Keywords: surge Froude number; 3D turbulent structures; air entrainment; free-surface perturbations; quadrant analysis; large eddy simulation; volume of fluid

Citation: Li, Z.; Venkateshwaran, A.; Karimpour, S. Turbulent Characteristics and Air Entrainment Patterns in Breaking Surge Waves. *Fluids* **2021**, *6*, 422. https://doi.org/10.3390/fluids6120422

Academic Editor: Martin Skote

Received: 2 November 2021
Accepted: 18 November 2021
Published: 23 November 2021

1. Introduction

Surge waves are transient open channel flows that form due to an abrupt change in flow depth or velocity. Surge waves appear in man-made hydraulic conveyance structures and natural systems. Tsunami waves, for instance, are generated by the displacement of water caused by landslides, volcanic activity, or earthquakes [1]. In man-made canals, surge waves are often initiated by the gate closure downstream [2]. One of the main characteristics of propagating surge waves and hydraulic jumps is the discontinuity in water depth and velocity across the wave front. These waves have been historically known to be analogous to shock waves in compressible flow [3] as both categories are compression waves of finite amplitude. This analogy is also founded on the basis of the similarity between shallow water equations and two-dimensional gas flow equations, as recently described by Karimpour and Chu [4,5].

Breaking surge waves are associated with Froude numbers ranging between 1.4 and 1.6 and higher, while smaller Froude numbers are linked to undular bores [6]. The breaking front of surge waves at high-surge Froude numbers has very complex dynamics, due to turbulence and air entrainment interactions. The turbulent characteristics across a breaking surge also contribute to sediment gathering, induce contaminant and debris transport, and cause bed erosion. Sediment entrainment and transport can in turn lead to a change in morphology along the propagation of the surge wave [7,8]. Shallow water hydraulics and the Method of Characteristics (MOC) provide reliable estimates of the phenomena by simulating the water and velocity in the streamwise direction (see, e.g., [1]). Nevertheless,

these models are incapable of capturing the dynamic surge front, as they assume the hydrostatic pressure distribution in depth.

The turbulence in a breaking surge wave is induced by two regimes. The surge toe separates two areas of distinct advective velocities upstream and downstream of the surge, while the surge moves with celerity. The velocity gradient excited by environmental perturbations leads to the formation of a shear layer originating at the surge toe [5,9,10]. The definition of the surge Froude number based on the coordinate system in translation with the surge wave [11] is analogous to the definition of the convective Froude number for shear layers [4]. The secondary regime that induces eddy generation is the breaking of the surge front [12,13].

The turbulent structures across the mixing layer and breaking surge are initiated due to velocity gradients in depth and pressure gradients in the streamwise direction. Although some of the structures are induced and initiated as two-dimensional, in time, they evolve into 3D structures [14,15]. Several numerical studies have investigated the turbulent structures and Reynolds stresses across breaking and undular surge waves. Many of these studies, however, have overlooked the 3D nature of the fully cascading turbulent flow across a breaking wave (e.g., [16]). Despite their intricate nature, only a few numerical studies have investigated the 3D nature of the rolling, breaking, and energy cascade in surge waves [13,15].

Due to the 3D nature of fully cascading eddies at the surge front, it is critical to capture the turbulent spanwise perturbations. Capturing this dimension requires delicate consideration of the spanwise scale of eddies. The extent of the spanwise boundary condition has a significant affect on the suppression of large-scale eddies, and it has to be selected to accommodate the largest scales [17]. Furthermore, most existing 3D numerical studies on surge waves use Large Eddy Simulation (LES). The performance of LES, however, significantly depends on the grid resolution and filter size [18]. Consideration of the impact of the spanwise boundary and LES filter resolution is often overlooked in many existing 3D studies on breaking surge waves [14,19].

In this study, we investigated the air entrainment patterns and their connection to the turbulent structures of breaking surge waves of Froude numbers higher than 1.6. Using a robust and accurate LES model, we resolved the majority of the large-scale perturbations, as suggested by Pope [18]. Furthermore, by applying a periodic boundary condition, we examined the role of spanwise perturbations in the formation of fully developed turbulent structures. Perturbation statistics are associated with the instability mechanisms that have been historically reported for breaking surge waves. The air entrainment patterns are reported and linked to the turbulent kinetic energy distribution in a breaking surge wave.

2. Methodology

We employed Open-source Field Operation and Manipulation (OpenFOAM) v7 to simulate the dynamic and transient turbulent characteristics of moving surge waves. We chose InterFoam, an incompressible multiphase solver employing the Volume-Of-Fluid (VOF) interface-capturing methodology for simulating free-surface flows. Furthermore, Large Eddy Simulation (LES) was employed to capture the larger than scale motions. While the energy containing eddies was captured in LES, the impact of smaller than scale motion was modeled using a subgrid-scale viscosity.

2.1. Governing Equation and Numerical Solutions

The governing equations for LES are derived by applying the convolution filter to the unsteady Navier–Stokes equations:

$$\frac{\partial \rho}{\partial t} + \frac{\partial (\rho \overline{u}_i)}{\partial x_i} = 0 \quad (1)$$

$$\frac{\partial(\rho\overline{u}_i)}{\partial t} + \frac{\partial(\rho\overline{u}_i\overline{u}_j)}{\partial x_j} = -\frac{\partial\overline{p}}{\partial x_i} + \mu\frac{\partial^2\overline{u}_i}{\partial x_j\partial x_j} + \frac{\partial\tau_{ij}^{SGS}}{\partial x_j}, \quad (2)$$

where $\overline{u}$ is the filtered velocity, $\overline{p}$ the filtered pressure, μ the dynamic viscosity, and $i, j = 1$, 2, 3 the x-, y-, z-directions, respectively. τ_{ij}^{SGS} represents the residual turbulent stress terms, from the Subgrid-Scale (SGS) perturbations, which are defined as:

$$\tau_{ij}^{SGS} = \rho\overline{u}_i\,\overline{u}_j - \rho\overline{u_iu_j} \quad (3)$$

By employing the Boussinesq hypothesis, the SGS turbulent stresses can be estimated as:

$$\tau_{ij}^{SGS} = -2\mu_t\overline{S}_{ij} + \frac{1}{3}\tau_{ii}^{SGS}\delta_{ij} \quad (4)$$

where δ_{ij} is the Kronecker delta and the strain rate $S_{ij} = \frac{1}{2}(\frac{\partial\overline{u}_i}{\partial x_j} + \frac{\partial\overline{u}_j}{\partial x_i})$. μ_t is the eddy viscosity of the SGS motions and is given by:

$$\mu_t = \rho C_k\Delta\sqrt{k_{SGS}} \quad (5)$$

where $C_k = 0.094$, k_{SGS} is the turbulent kinetic energy in the subgrid scale, and Δ is the filter size. The k_{SGS} is calculated using the following transport equation [20]:

$$\frac{\partial(\rho k_{SGS})}{\partial t} + \frac{\partial(\rho\overline{u}_i k_{SGS})}{\partial x_i} = \frac{\partial}{\partial x_i}[(\mu+\mu_t)\frac{\partial k_{SGS}}{\partial x_i}] - \rho\tau_{ij}^{SGS}\overline{S}_{ij} - C_\epsilon\frac{\rho k_{SGS}^{3/2}}{\Delta} \quad (6)$$

where $C_\epsilon = 1.04$. The transport model proposed by Yoshizawa and Horiuti [20] was applied to ensure that the subgrid viscosity was small in laminar and shear flows and was not as dissipative as the well-known Smagorinsky eddy viscosity.

To capture the interface between water and air, the VOF was used. The fluid properties in this method are estimated using the fractional fluid volume in each cell. For current simulation for 2-phase air and water flow, based on the water and air volume fractions, α_w and $\alpha_a = 1 - \alpha_w$, the combined phase density and viscosity is defined as:

$$\rho = \rho_w\alpha_w + \rho_a(1-\alpha_w); \;\; \mu = \mu_w\alpha_w + \mu_a(1-\alpha_w) \quad (7)$$

The phase distribution for α_w can be determined from [21]:

$$\frac{\partial\alpha_w}{\partial t} + \frac{\partial(\overline{u}_i\alpha_w)}{\partial x_i} + \frac{\partial}{\partial x_i}[u_{ci}\alpha_w(1-\alpha_w)] = 0 \quad (8)$$

In Equation (8), the third term is an artificial compression term, intended to sharpen the interface [22], where u_{ci} represents the relative velocity for water and air and given by:

$$u_{ci} = C_\alpha\frac{|u|}{|\nabla\alpha_w|}\frac{\partial\alpha_w}{\partial x_i} \quad (9)$$

where C_α represents the compression strength and the recommended value for $C_\alpha = 1$ [23].

While the temporal discretization is semi-implicit, we employed different spatial discretization schemes for the convection terms. The convection terms appear in the momentum, k_{SGS} transport, as well as phase equation, and spatial discretizations were performed based on the sensitivity and the nature of these terms, as discussed below. The discretization of the subgrid-scale turbulent kinetic energy flux, k_{SGS}, appearing in Equation (6), was performed using a first-order upwind biased interpolation. However, the advection flux in the momentum equation requires a higher-order approximation, and therefore, an upwind biased central differencing was selected. On the other hand, for the flux of phase, α_w, in Equation (8), the Van Leer Total Variation Diminishing (TVD) method

was selected. This TVD scheme is second-order accurate and is bounded, and its accuracy can drop to as low as first order in regions with discontinuity. As demonstrated in Figure 1, starting from its initial condition, the moving surge wave exhibits discontinuity in phase at the surge front, and it requires a TVD scheme, or an alternative, to ensure numerical stability and accuracy [4,23]. The pressure–velocity coupling in the Navier–Stokes equations was conducted using the PIMPLE algorithm [24].

2.2. Computational Domain and Flow Conditions

A three-dimensional computational domain was designed as shown in Figure 1a. In order to achieve fully developed turbulent flow across a breaking surge wave, we implemented a periodic boundary condition in the spanwise z-direction. This technique is used in open-channel flow (see, e.g., [25]) and in other flow types [17] to produce a fully developed turbulent flow, where the perturbations are fed back into the domain. The size of the periodic domain width, T, however, should be selected so that it is several times larger than the largest flow scale in the domain [17]. The turbulent scale, however, is not studied for breaking waves. Therefore, in order to fully capture all turbulent scales, including large scales, we implemented multiple domain width sizes, T, and assessed the role of the domain width on the growth of spanwise turbulent fluctuations.

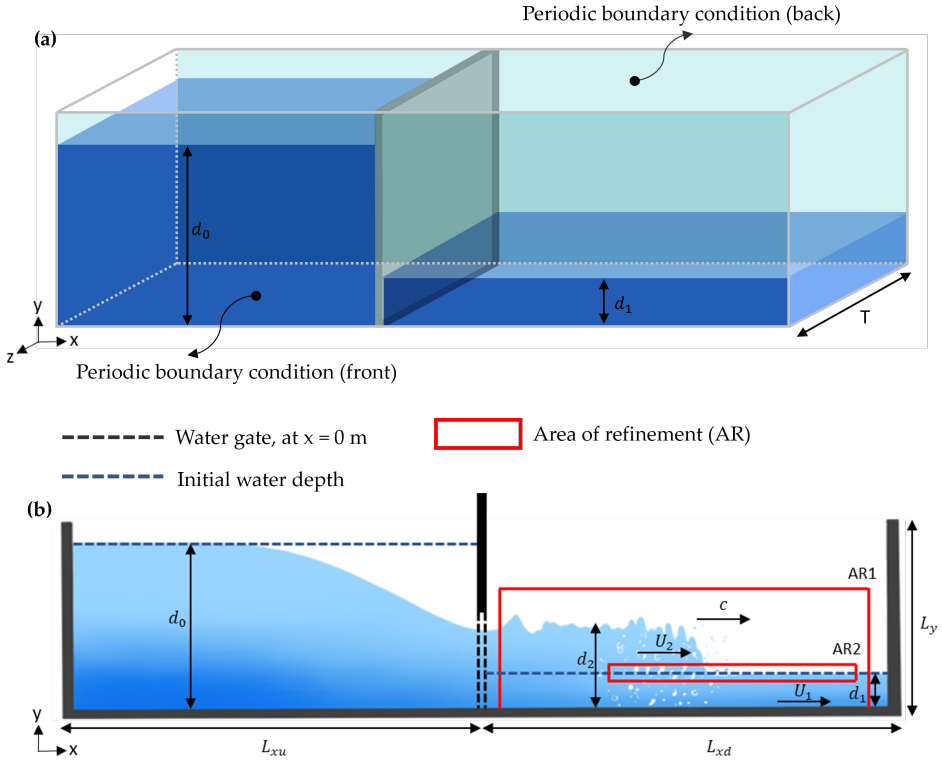

Figure 1. Sketch of the computational domain: (**a**) 3D and (**b**) 2D side view.

The top face was set to open air by assigning an atmospheric boundary condition, and the rest of the three faces were rigid, where smooth boundary conditions were applied. Table 1 summarizes the geometry, flow, and initial conditions used in this paper. The initial water depths in the upstream and downstream of the gate, d_0 and d_1, were designed based on the Method of Characteristics (MOC). Using this analytical method, the breaking wave celerity, c, was also estimated. The surge Froude number, Fr_s, is defined as:

$$Fr_s = \frac{c + U_1}{\sqrt{g d_1}} \tag{10}$$

where in this study, $U_1 = 0$. Based on the MOC, Chanson [2] proposed the following expression for the surge Froude number, Fr_s:

$$Fr_s = \frac{c}{\sqrt{gd_1}} = \frac{0.63545 + 0.3286(\frac{d_1}{d_0})^{0.65167}}{0.00251 + (\frac{d_1}{d_0})^{0.65167}} \quad (11)$$

As suggested by Leng and Chanson [6], among others, breaking surge waves with stronger turbulent characteristics correspond to surge Froude numbers of $Fr_s > 1.4$–1.6. The initial conditions outlined in Figure 1 and Table 1 were designed to induce the formation of breaking waves with higher Froude numbers outside of this range. The surge wave celerity, c, varies slightly from 2.93 m/s to 2.98 m/s for $Fr_s = 1.71$ and 2.13, respectively. The computational domain in the x-direction was stretched to $L_{xd} = 24$ m, downstream of the gate, to ensure that wave reflection from the downstream boundary did not occur prior to the end of simulation at $t = 8$ s. Similarly, the upstream stretch, L_{xu}, was $L_{xu} = 25$ m, to avoid the reflection of negative characteristics from the upstream rigid boundary. The domain size in the y-direction was kept at $L_y = 1.2$ m in all simulations.

A mesh size of $\Delta x = 0.01$ m was applied. However, as explained by Karimpour et al. [26], a finer resolution is required to capture the larger-than-scale perturbations in an LES model. To ensure proper assessment of larger-than-scale perturbations and the Turbulent Kinetic Energy (TKE), we performed a series of mesh sensitivity analyses. Our assessment showed the necessity of two Areas of Refinements (ARs): AR1, which was designed to contain the propagation area of the positive surge wave, and AR2 in the vicinity of the surge toe, both illustrated in Figure 1b. In AR1, the grid was refined to $dx_1 = 0.005$ m. To capture the smaller-scale perturbations induced by the shear velocity in AR2, the grid was further refined to $dx_2 = 0.0025$ m. In Cases 1 and 2-3, the 3D computational domains were discretized to more than 82 million computational grids. Further discussion of the subgrid-scale resolution is presented in the Results Section.

Table 1. Domain geometry and flow conditions.

ID	d_1 (m)	d_0 (m)	c (m/s)	d_2 (m)	AR1 (m^2)	dx_1 (m)	AR2 (m^2)	dx_2 (m)	Fr_s	T (m)
1	0.3	1.0	2.93	0.596	$22 * 0.7$	0.0050	$6.95 * 0.1$	0.0025	1.71	$40\Delta x$
2-1	0.2	1.0	2.98	0.513	$22 * 0.6$	0.0050	$7.30 * 0.1$	0.0025	2.13	$10\Delta x$
2-2	0.2	1.0	2.98	0.513	$22 * 0.6$	0.0050	$7.30 * 0.1$	0.0025	2.13	$20\Delta x$
2-3	0.2	1.0	2.98	0.513	$22 * 0.6$	0.0050	$7.30 * 0.1$	0.0025	2.13	$40\Delta x$

3. Results

The computational domain was designed to accommodate 8 s of simulation before the positive and negative characteristics were affected by the rigid upstream and downstream boundaries. During the first 4 s, for both Froude numbers, the surge wave fronts were not fully developed and, therefore, were excluded from the current analysis. The results were obtained by using 100 ensembles between $t = 4$ s and 6 s, when the turbulence at the wave front was fully developed.

3.1. Subgrid-Scale Resolution

One of the primary functions of an LES model is to dissipate the energy from the resolved scales at an appropriate rate. A critical consideration for LES is the selection of the filter size that can resolve the majority of large-scale energy-containing eddies. A general and widely used method to estimate the quality of LES results was introduced by Pope [18], who suggested that the resolved TKE, denoted by k_{res}, should be more than 80% of the total TKE to enable a well-resolved simulation. Matheou and Chung [27], on the other hand, recommended resolving at least 90% of the TKE for the reliable prediction of the mean statistics.

To estimate the percentage of the resolved turbulent kinetic energy, k_p, two parameters need to be determined first: the subgrid-scale TKE, k_{SGS}, directly modeled using Equation (6), and the resolved TKE, k_{res}. The resolved TKE presents the energy in larger-than-scale turbulent motion and is defined as:

$$k_{res} = \frac{1}{2}(\overline{u'u'} + \overline{v'v'} + \overline{w'w'}) \tag{12}$$

where u', v', and w' are the resolved velocity perturbation components in the x-, y-, and z-directions, respectively. Furthermore, $\overline{u'u'}$, $\overline{v'v'}$, and $\overline{w'w'}$ are the normal stresses in the Reynolds stress tensor. For a moving surge wave, with phase discontinuity at the surge front, estimating the velocity perturbations requires the consideration of the transient nature of the surge wave. The celerity of the surge waves here closely resembled the averaged celerity estimated by the MOC. Therefore, to estimate the perturbation components, all profiles were shifted with a spatial lag of $x_{lag} = c/t$ in the streamwise x-direction. All profiles were shifted, and therefore, were projected to the vicinity of the gate at $t = 0$ s. The details of this spatial projection are given in Appendix A. The percentage of resolved TKE, k_p, is calculated as:

$$k_p = \frac{k_{res}}{k_{res} + k_{SGS}} \tag{13}$$

The VOF method accounts for both phases, and herein, the phase separation that delineates the free-surface was identified at $\alpha_w = 0.5$. Splash and separation were not accounted for in delineating the free-surface shown in Figure 2 in black. Figure 2a,b shows larger-than-scale TKE, k_{res}, for $Fr_s = 1.71$ and 2.13, respectively. Higher values in these plots are observed around the surge front in both air and water, but this also spreads in depth and extends between the surge heel and toe. Furthermore, k_{res} peaks in the vicinity of the surge toe for both Froude numbers. Existing laboratory experiments [28,29] have also shown a sharp rise in the normal Reynolds stresses, $\overline{u'u'}$ and $\overline{v'v'}$, as components of the TKE, near the toe. Figure 2c,d shows the plots of the instantaneous subgrid-scale TKE, k_{SGS}, and exhibit darker colors and intensities around the toe and surge front. Due to the higher k_{SGS} around the toe, the ratio of resolved to total TKE was at the lowest value of about 86% in this area. However, this ratio remained above the recommended value for LES [18]. In the surge front, the ratio of k_p remained consistently above 90%. This indicated that the LES model resolved mostly 90% of the TKE. This was achieved by designing two areas of refinement, in the surge propagation area (AR1) and further refinement across the toe (AR2), where the shear layer formed. The k_{SGS} transport equation does not treat the near-wall, nor was the near-wall region refined to resolve the very small scales. Therefore, this area had very low k_p. However, as shown in the later sections, the lower envelope of mixing in the breaking surge was not affected by the near-wall region, and therefore, this did not impact the development of turbulent structures in the vicinity of the surge front.

3.2. Water Depth Perturbations

Figure 3a,b shows the instantaneous water surface profiles, all in grey, and the averaged water surface profile in blue. Since the averaged water depth changes in the x-direction, this spatially varied averaged water depth was used for normalization. The magnitude of the normalized water surface perturbation, or the squared root mean square (rms), ${h'_{rms}}^2/\overline{h}^2 = \overline{h'^2}/\overline{h}^2$, was calculated and is plotted in Figure 3c,d for $Fr_s = 1.71$ and 2.13 for $T = 40\Delta x$, respectively. The normalized water surface perturbation peaked at ${h'_{rms}}^2/\overline{h}^2 = 0.008$ for $Fr_s = 1.71$ and reached 0.011 at the higher Froude number of $Fr_s = 2.13$. Leng and Chanson [29] summarized several experimental works of both surge wave and hydraulic jump studies about the relation between the Froude number, Fr_s, and the maximum water depth perturbations, h'_{max}. In general, h'_{max} increases with Fr_s, and our maximum water depth perturbation followed the same trend from $Fr_s = 1.71$ to 2.13. In both cases, this peak was observed immediately behind the toe.

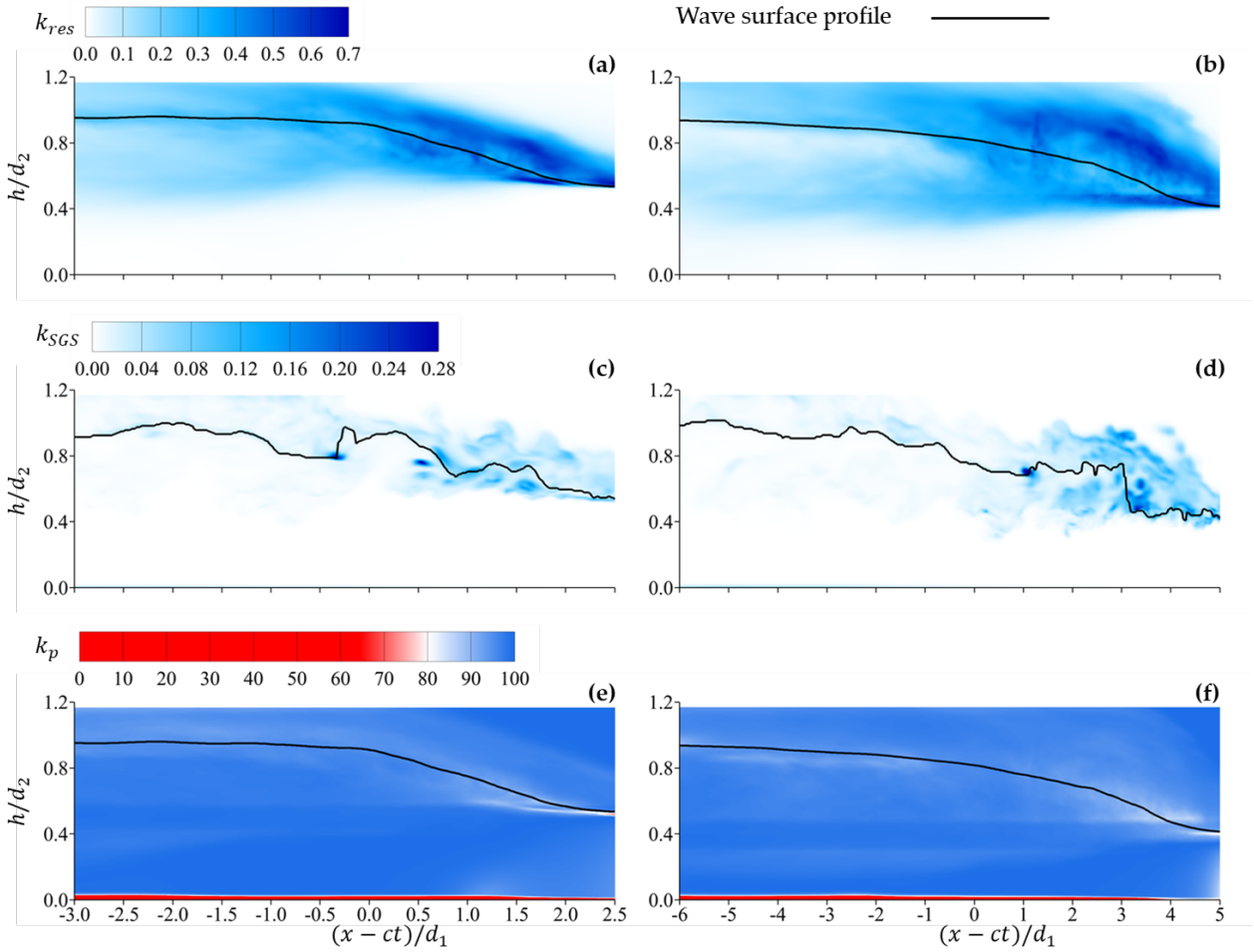

Figure 2. Plots of (**a**,**b**) time and z-averaged k_{res}; (**c**,**d**) k_{SGS} at $t = 4.2$ s and $z = 0.02$ m; (**e**,**f**) time and z-averaged k_p with 80% as the threshold, for Case 1 with $Fr_s = 1.71$ (left column) and Cases 2-3 with $Fr_s = 2.13$ (right column), respectively. For $Fr_s = 1.71$, the averaged position of the surge toe is approximately observed at $(x - ct)/d_1 = 2.0$, and the surge wave extends to $(x - ct)/d_1 = 0.0$. For $Fr_s = 2.13$, the toe is positioned at $(x - ct)/d_1 = 4.0$, and the averaged profile of the surge wave extends to $(x - ct)/d_1 = 0.0$.

Higher moments of perturbation, skewness, S_ϕ, and kurtosis, K_ϕ, provide deeper insight into the distribution of the perturbation and ultimately the physics of the flow. The skewness is the third moment and kurtosis is the fourth moment of perturbation of parameter ϕ, where ϕ can be velocity components, pressure, and water depth and are defined as:

$$S_\phi = (\overline{\phi'^3})/(\overline{\phi'^2})^{3/2};\ K_\phi = (\overline{\phi'^4})/(\overline{\phi'^2})^2 \tag{14}$$

where $\phi' = \phi - \overline{\phi}$. The skewness reveals information about the asymmetry of the perturbation, while kurtosis provides information on the flatness of the perturbation distribution. The skewness for a Gaussian distribution is around zero, and a positive skewness means that the perturbation is more likely to take on large positive values than large negative values. On the other hand, the kurtosis for a Gaussian distribution is around three. Perturbation measurements leading to a kurtosis lower than this value are mainly clustered around the mean, whereas perturbation measurements dominated by intermittent extreme events have a higher kurtosis.

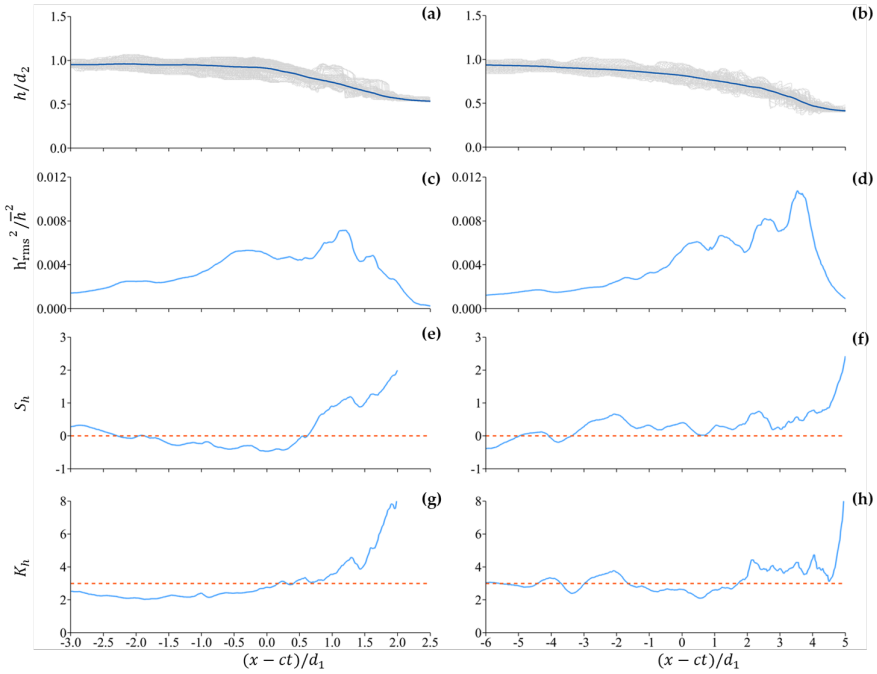

Figure 3. Normalized water surface perturbation analysis: (**a**,**b**) time and z-averaged wave surface, where the blue line is the averaged water surface profile, $\bar{h}/d_2$, and the grey lines denote instantaneous water surface profiles, h/d_2; (**c**,**d**) root mean square (rms) of surface perturbation, ${h'_{rms}}^2/\bar{h}^2$, $h' = h - \bar{h}$; (**e**,**f**) skewness of h, S_h; (**g**,**h**) kurtosis of h, K_h, for Cases 1 with $Fr_s = 1.71$ (left column), and Cases 2-3 with $Fr_s = 2.13$ (right column), respectively.

Around the heel, the depth skewness remained close to zero for both Froude numbers, as shown in Figure 3e,f. However, moving from the heel towards the toe, the skewness started to rise and reached approximately 2.0 and 2.5 around the toe for $Fr_s = 1.71$ and 2.13, respectively. This showed the tendency of the water surface profile perturbation to experience extreme positive events, where the instantaneous water surface most likely exceeded the average profile. The water surface kurtosis profiles for both Froude numbers are shown in Figure 3g,h. In the vicinity of the heel at $(x - ct)/d_1 = 0$, the kurtosis was $K_h \approx 3$; however, it rose to above three close to the toe. This confirmed that the flow mainly comprised intermittent extreme water depth perturbations around the toe.

3.3. Air Entrainment Profiles and Mixing Cones

Two mechanisms have been identified in the literature that contribute to the instability and development of a highly turbulent front in a surge wave. These are the advective–diffusion region and the breaking front [9]. The first instability is induced by the velocity gradient at the surge toe [5] and the second by the phase discontinuity at the surge front. The formation of this breaking region is independent of the inflow conditions and is dependent on the surge height [30].

Figure 4a–d shows plots of the instantaneous air concentration distribution (the left column $Fr_s = 1.71$ and the right column $Fr_s = 2.13$). The orange lines in these profiles delineate the marginal zero value for eddy viscosity, $\nu_t = \mu_t/\rho = 0.00001$ m^2/s. Along with the water surface profiles, these lines provide an envelope where the mixing is confined. In Figure 4e,f, the averaged air concentration and the upper and lower envelopes, y_s and y_b, are plotted for $Fr_s = 1.71$ (left) and 2.13 (right). The averaged lower envelope of air entrainment, y_b, is plotted using both eddy viscosity and $\alpha_w = 0.5$. Both methods yielded similar lower envelopes for both Froude numbers. Furthermore, the instantaneous and averaged lower envelopes demonstrated the proximity of the shear layer to the rigid bed. In all cases, this lower envelope developed at a depth, where the impact of the boundary layer was not present. This evidently indicated that low k_p values for the near the boundary

region, shown in Figure 2e,f, had no effect on the development of the turbulent region across the surge front, between the surge toe and the heel.

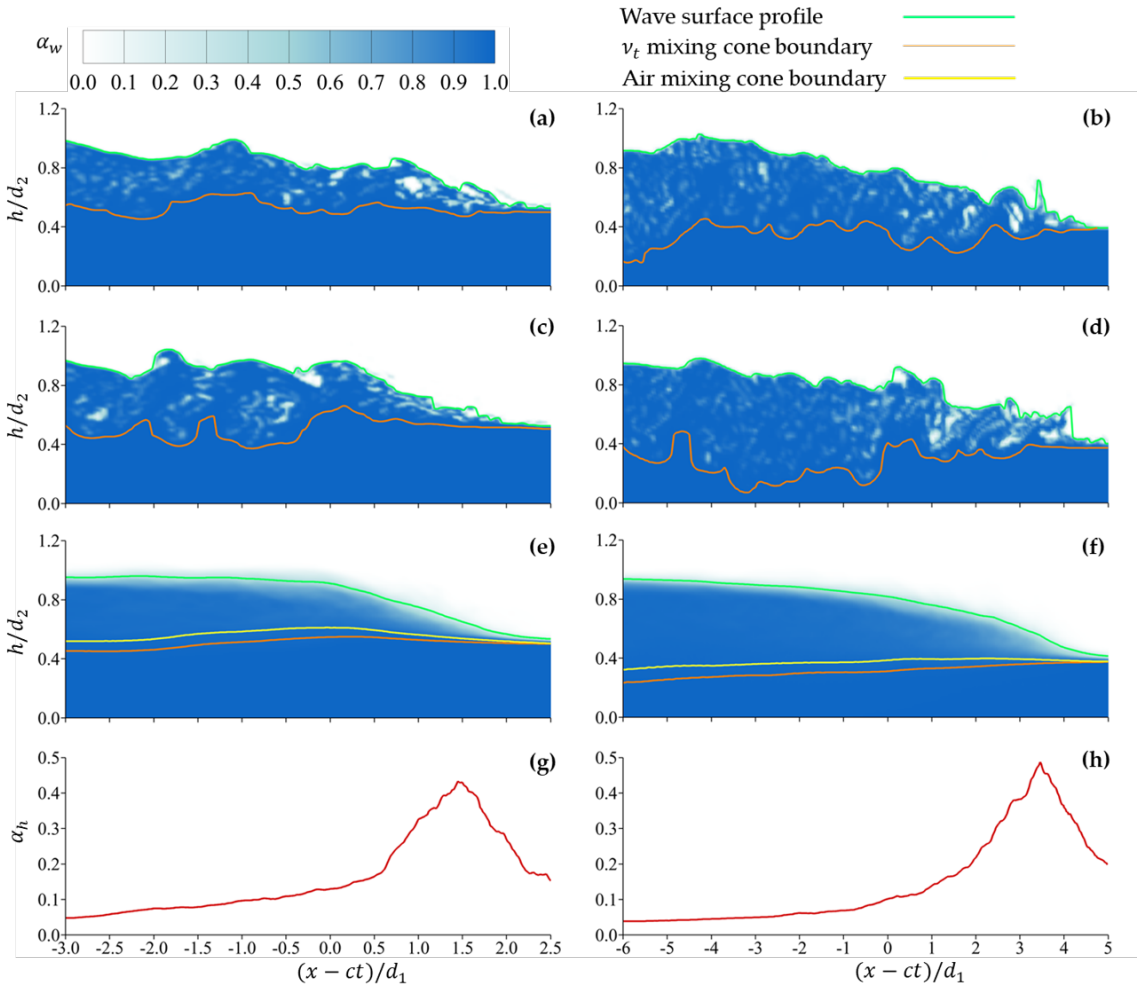

Figure 4. Normalized wave surface, v_t mixing cone boundary, and air mixing cone boundary plots for: (**a**,**b**) at $t = 4.0$ s, $z = 0.2$ m; (**c**,**d**) at $t = 4.5$ s, $z = 0.2$ m; (**e**,**f**) time and z-averaged; (**g**,**h**) α_h, for Cases 1 with $Fr_s = 1.71$ (left column) and Cases 2-3 with $Fr_s = 2.13$ (right column), respectively.

Instantaneous and averaged upper and lower bounds, as well as the air concentration contours indicated that the extent of air entrainment grew with the Froude number, which was previously reported by Wüthrich et al. [31]. To quantify the air entrainment across the surge wave, the average air concentration, α_h, is defined between the free-surface profile at y_s and the lower boundary of the mixing cone in the advective–diffusion region denoted by y_b:

$$\alpha_h = \sum_{y_b}^{y_s} \alpha_a / \sum_{y_b}^{y_s} \alpha_w \tag{15}$$

The peak value for average air concentration, α_h, shown in Figure 4h, occurred at $x - ct = 3.4d_1$ for $Fr_s = 2.13$, which coincided with the peak of surface perturbation plotted in Figure 3d. This is supported by the plot of k_{res} for this Froude number in Figure 2b. The area of high larger-than-scale perturbation in Figure 2b intersects with the free-surface right behind the toe, leading to substantial levels of air entrainment near the toe. However, the contour implies that the area with intense resolved TKE, k_{res}, deviated from the free-surface moving upstream away from the toe. This plot also demonstrates that the intensity of the resolved TKE reduced behind the toe. These phenomena combined led to rapid induction of air entrainment close to the toe, and subsequently reduction in air entrainment, moving

further upstream. A similar pattern was observed for $Fr_s = 1.71$. Chanson [32] conducted laboratory experiments to study air entrainment in surge waves by generating dam-break waves. They reported a very high air concentration ratio near the toe, which agrees with our observation for α_h.

Air concentration, α_a, is also plotted against depth, vertical y coordinate, at multiple locations between the surge toe and heel in Figure 5. Here, three instantaneous profiles, as well as the averaged profiles are plotted. The air concentration pattern in depth in the shear layer and breaking region has been reported in the literature for hydraulic jumps [9,33]. The air entrained at the toe was advected and diffused in the shear layer. The instantaneous profiles often peaked at the depth of the shear layer, for instance for $h/d_2 = 0.42$ at $(x - ct)/d_1 = 3.505$ (Figure 5c) and $h/d_2 = 0.48$ at $(x - ct)/d_1 = 2.505$ (Figure 5b), for $t = 4.25$ s. While this trend was not observed at all times, the averaged profiles also seemed to peak where the shear layer formed. The position of this local maximum occurred at slightly higher depths as the profiles moved away from the toe, which is consistent with data reported by [33]. Afterwards, α_a grew with the depth and reached one at the free-surface. This demonstrated the importance of the TKE across the shear layer in air entrainment and the air distribution, as observed in Figure 4g,h.

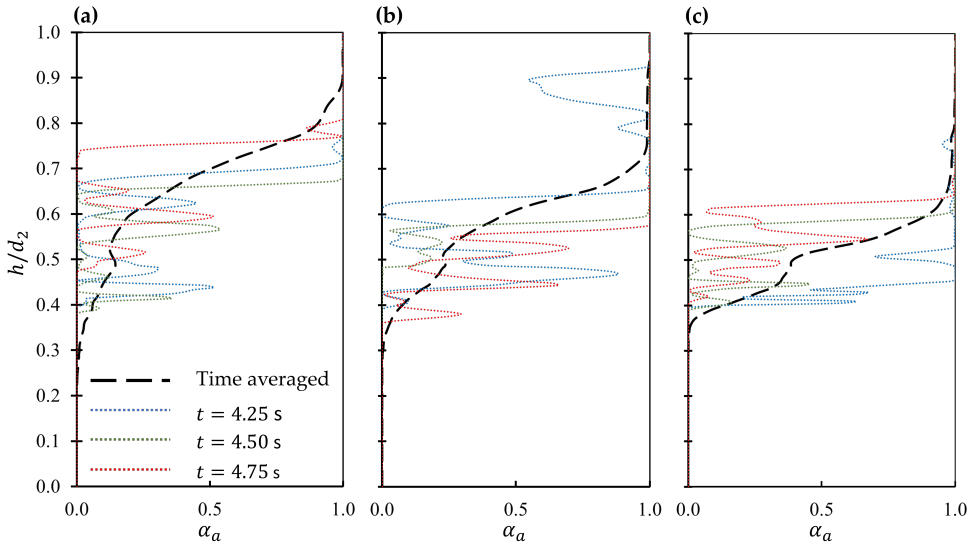

Figure 5. Plots of instantaneous α_a against h/d_2 for $t = 4.25$ s, 4.50 s, 4.75 s, and averaged α_a at (**a**) $(x - ct)/d_1 = 1.505$, (**b**) $(x - ct)/d_1 = 2.505$, and (**c**) $(x - ct)/d_1 = 3.505$ for $Fr_s = 2.13$ (Cases 2-3).

3.4. Velocity Perturbations and Quadrant Analysis

To quantify the turbulent structures behind breaking surge waves, the instantaneous perturbations were extracted and are plotted in Figure 6. These plots were produced at two depths: at $y = d_1$ for points located behind the surge toe and for those located at the midpoint of surge height at $y = d_1 + 0.5(d_2 - d_1)$. Standard Deviational Ellipses (SDEs) are also plotted at 99% and 50%. SDEs delineate the spatial characteristics and distribution of perturbations. The orientation of the SDEs was such that the semi-axes align with the eigenvectors of the covariance matrix of the sample. The plotted SDEs approximate the regions containing 99% and 50% of the perturbations in each perturbation cloud. Quadrant analysis is one of the most conventional methods to identify the dominant coherent structures in a turbulent flow [34,35].

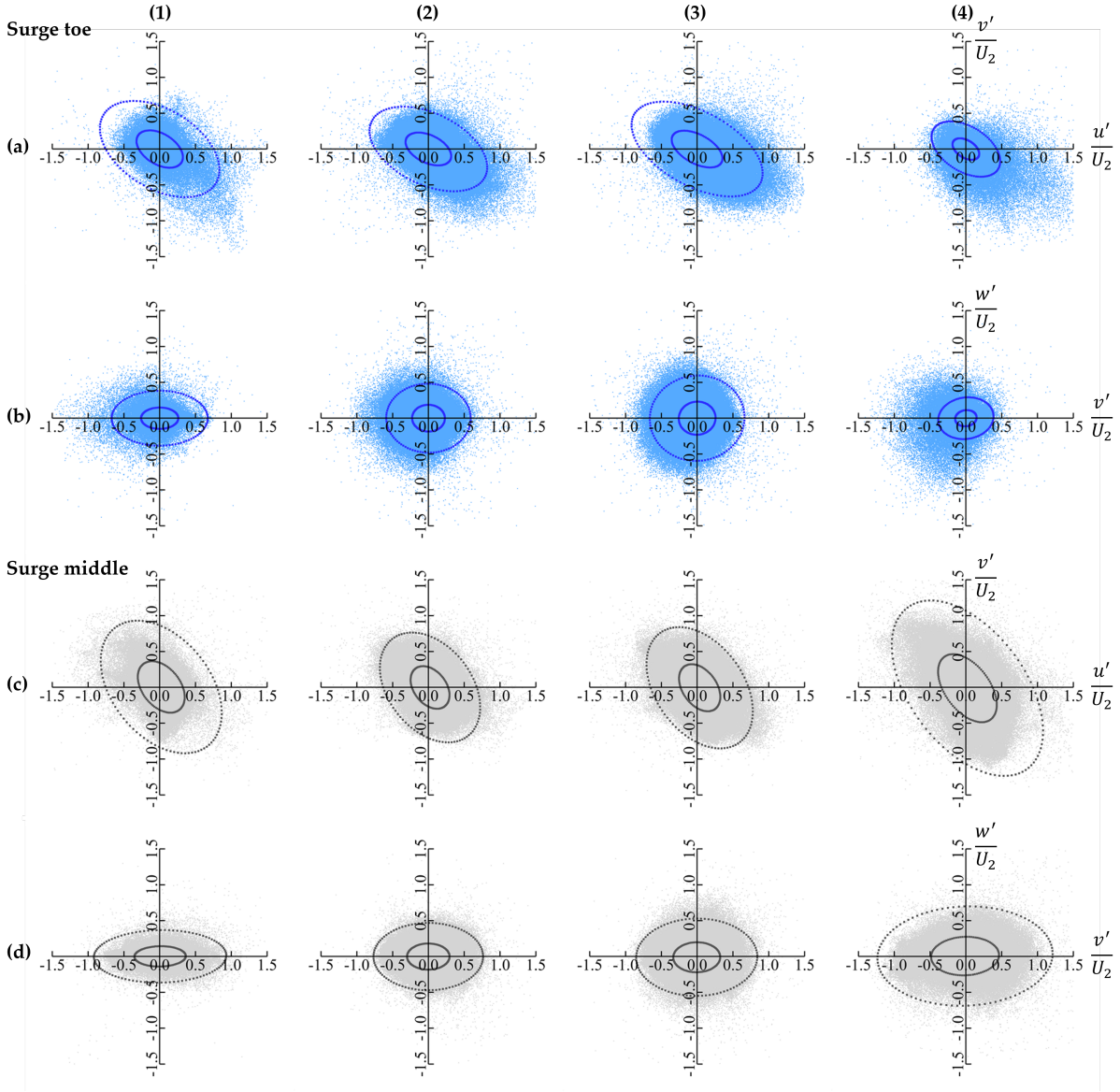

Figure 6. Velocity perturbation plots normalized by U_2. (**a**,**c**) are u'/U_2 vs. v'/U_2; (**b**,**d**) are v'/U_2 vs. w'/U_2 at $y = d_1$ and $= d_1 + 0.5(d_2 - d_1)$, respectively. Column (1) is for Cases 2-1 with $T = 10\Delta x$ and $Fr_s = 2.13$; Column (2) for Cases 2-2 with $T = 20\Delta x$ and $Fr_s = 2.13$; Column (3) for Cases 2-3 with $T = 40\Delta x$ and $Fr_s = 2.13$; and Column (4) for Cases 1 with $T = 40\Delta x$ and $Fr_s = 1.71$. The velocity perturbations are extracted for points located between $(x - ct)/d_1 = 0$ and the surge front.

In order for us to assess the proper periodic domain size in the z-direction, we conducted the simulation for $Fr_s = 2.13$ for three domain sizes of $T = 10\Delta x$, $20\Delta x$, and $40\Delta x$, in Cases 2-1, 2-2, and 2-3, respectively. The plotted perturbations in Figure 6 in Columns 1 to 3 represent the progression of perturbation as we expanded the domain in the z-direction. As seen in the plot of v'/U_2 against w'/U_2 in $T = 10\Delta x$ in Figure 6(b1), in this narrow domain, v'/U_2 was dominant over w'/U_2. However, progressively, as we expanded the domain, the SDEs became closer in shape to concentric circles, suggesting a comparable magnitude for v'/U_2 and w'/U_2. From $T = 20\Delta x$ to $40\Delta x$, the impact of the domain width became negligible, as shown in Figure 6(b2,b3). The structure of the perturbations became invariant to the domain width at $T = 40\Delta x$. This width, therefore, was selected as the optimal domain size to demonstrate the structure of perturbations in this paper.

The perturbations in the xy-plane at $y = d_1$ and $T = 40\Delta x$, u'/U_2 and v'/U_2 are plotted for $Fr_s = 2.13$ and 1.71 in Figure 6(a3,a4), respectively. The 99% and 50% confidence

SDEs in both Froude numbers are inclined towards the second and the fourth quadrant. In Quadrants 2 and 4, the product of perturbations in the x- and y-directions, $u'v'$, is negative. This consequently led to a positive production of the TKE. The xy perturbation cloud was dominated by sweeps (demonstrated by perturbations in Quadrant 4) and ejections (Quadrant 2) [34]. A similar pattern emerged at different depths across the surge height, as plotted for $y = d_1 + 0.5(d_2 - d_1)$ in Figure 6(c3,c4).

On the contrary, the yz perturbation cloud illustrated a different pattern. Figure 6(b3,b4) shows the even distribution of perturbations in all four quadrants. All four mechanisms of outward interactions (Quadrant 1), sweeps (Quadrant 2), inward interactions (Quadrant 3), and ejections (Quadrant 4) became equally significant. This indicated that the overall product of perturbations in the yz-plane was zero, leading to no turbulent production. A similar trend appeared at $y = d_1 + 0.5(d_2 - d_1)$, where the SDEs for v'/U_2 versus w'/U_2 perturbations spread equally in all four quadrants, as illustrated in Figure 6(d3,d4). Evidence arising from instability mechanisms is discussed in the following section to substantiate this observation.

3.5. Q-Criterion Analysis and Relation to Production

The quadrant analysis was well supported by the vortex structure observed in the breaking surge wave. Due to the complexity of the flow, with multiple instability-inducing mechanisms, the plot of vorticity alone does not shed light on the vortical circulations, also reported by Lubin and Glockner [15]. Instead, the Q-criterion was used to visualize the formation, rolling, and merging of the coherent structures.

This criterion was introduced by Hunt et al. [36], and it is defined in terms of the instantaneous velocity gradients. A positive value for the Q-criterion identifies rotation-dominated regions of the flow, or vortices. Similarly, negative values are associated with straining regions of the flow. Figure 7 is the plot of the Q-criterion and Q isosurfaces (at Q = 2000) in the xy-plane for $Fr_s = 2.13$ and 1.71 for $T = 40\Delta x$. Figure 7a,b,e,f shows the instantaneous Q-criterion contour plots, and Figure 7c,d,g,h shows the instantaneous Q isosurfaces at Q = 2000. These plots outline the change of coherent structures in time for two Froude numbers. Despite changes in the instantaneous distribution of Q, these plots consistently show the accumulation of vortices adjacent to the toe and behind the breaking surge front. The vortices were generated by the two instability mechanisms outlined earlier and were advected behind the surge. Since the shear instability was in the xy-plane (the gradient of the x-component of the velocity in the y-direction), the vortices in the vicinity of the toe were expected to have a 2D structure. Similarly, the instability caused by the depth discontinuity also occurred in the xy-plane (phase or depth gradient across the surge front in the x-component). The velocity perturbation component in the z-direction, w', was, however, critical for fully cascading turbulent flow an comparable in size to the velocity perturbation component in the y-direction, v', as demonstrated in Figure 6b,d.

Figure 8 contains the instantaneous plots of the Q-criterion in the yz-plane. As evident here, the coherent structures were present in the yz-plane. The width of the domain, $T = 40\Delta x$, as shown in all instances for both Froude numbers of $Fr_s = 1.71$ in Figure 8a,b and $Fr_s = 2.13$ in Figures 8c,d, was significantly larger than the scale of eddies formed in the yz-plane. This ensured that the domain size did not suppress the perturbation growth in the z-direction, and therefore, 3D structures were not suppressed. Despite their role in the 3D structures, the yz-perturbations did not contribute to the production of turbulence as discussed in the quadrant analysis.

To further illustrate the results presented above, a video demonstration of the evolution of the Q isosurfaces at Q = 2000 in time is available in the Supplementary Material for both Froude numbers of $Fr_s = 1.71$ (Case 1) and 2.13 (Cases 2-3).

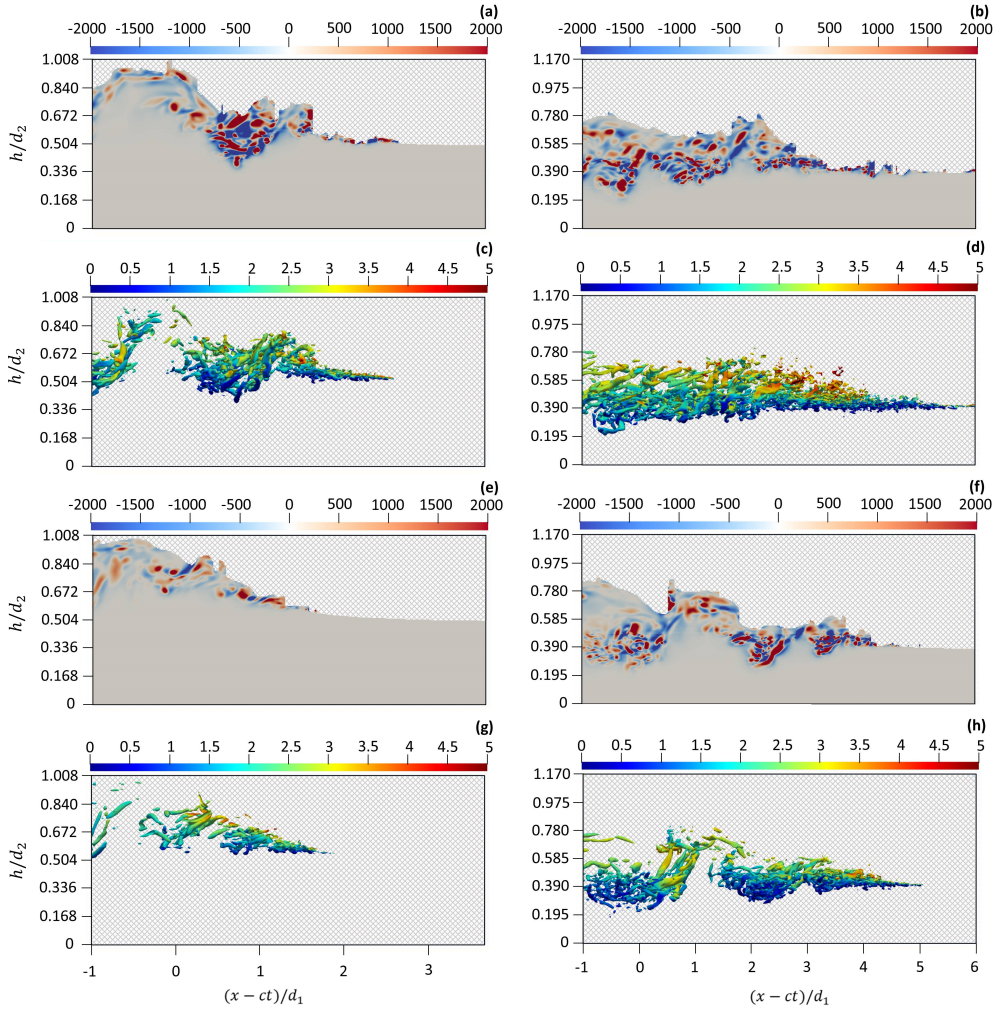

Figure 7. Plots of the instantaneous Q-criterion contour and Q = 2000 isosurfaces on the xy-plane at z = 0.2 m. The isosurfaces are colored with the resultant velocity. (**a**,**b**) are Q contours for $t = 4.25$ s; (**e**,**f**) for $t = 4.75$ s for $Fr_s = 1.71$ (left column) and $Fr_s = 2.13$ (right column) for $T = 40\Delta x$. Similarly, (**c**,**d**) are isosurfaces for $t = 4.25$ s and (**g**,**h**) for $t = 4.75$ s for $Fr_s = 1.71$ (left column) and $Fr_s = 2.13$ (right column), respectively.

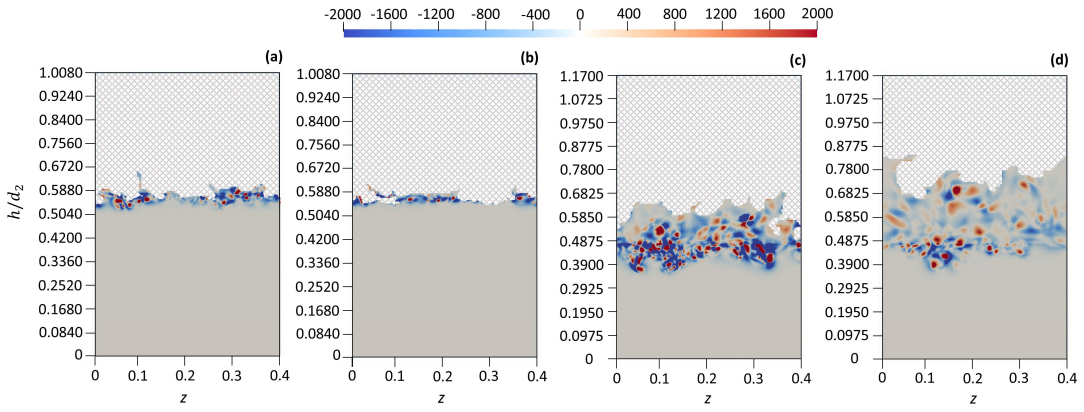

Figure 8. Plots of the Q-criterion contour on the yz-plane at $(x - ct)/d_1 = 1.5$ for $Fr_s = 1.71$ (Case 1) at (**a**) $t = 4.25$ s and (**b**) $t = 4.75$ s. Similar Q contour plots are presented for $Fr_s = 2.13$ (Cases 2-3) at (**c**) $t = 4.25$ s and (**d**) $t = 4.75$ s.

4. Conclusions

In the scope of this paper, we investigated the turbulent structures across breaking surge waves, highlighted the 3D behavior of velocity perturbations, and examined their linkage with the instability mechanisms in breaking surge waves. We conducted a series of numerical simulations of breaking surge waves with Froude numbers of $Fr_s = 1.71$ and 2.13, using a large eddy simulation three-dimensional model. By implementing a Volume Of Fluid (VOF) solver, we accounted for air entrainment and the linkage with the coherent structures across the surge wave. In a highly turbulent breaking surge, two mechanisms contributed to the instability: the formation of the shear layer, due to the velocity gradient, at the toe, and wave breaking at the air–water interface due to phase discontinuity. Our analysis of the water surface perturbation patterns, including higher moments, indicated extreme water surface perturbations near the toe. This was attributed to the steep wave front and the high level of Turbulent Kinetic Energy (TKE) at the toe. The simulation also produced air concentration profiles consistent with the data obtained from existing laboratory observations.

Furthermore, our analysis highlighted the role of spanwise perturbations in the development of fully developed turbulent structures behind the surge wave. Using a periodic boundary condition, we ensured that the domain size did not constrain the growth of spanwise perturbations. The Standard Deviational Ellipses (SDEs) in the xy velocity perturbation cloud for both Froude numbers were oriented towards the second and fourth quadrants, leading to positive TKE production. The yz velocity perturbations demonstrated that the magnitude of the spanwise perturbations were comparable to other perturbation components. The SDEs, however, suggested that yz perturbations do not contribute to the TKE production. The appearance of the TKE production in the xy-plane alone was attributed to the formation of both instability mechanisms in this plane. Our perturbation analysis also illustrated the role of spanwise perturbation in the distribution of TKE and the evolution of the three-dimensional turbulent structure in a breaking surge wave. To illustrate the three-dimensional structure, further work is required to study the isotropic behaviors near the surge front, behind the surge, and in the toe region.

Supplementary Materials: Supplementary videos are available online at https://www.mdpi.com/article/10.3390/fluids6120422/s1.

Author Contributions: Conceptualization, S.K.; Introduction and Methodology S.K. and Z.L.; numerical simulation, Z.L.; formal data analysis, Z.L. and A.V.; discussion, S.K. and Z.L.; writing—original draft preparation, Z.L.; writing—review and editing, S.K.; visualization, Z.L. and A.V.; supervision, S.K. All authors have read and agreed to the published version of the manuscript.

Funding: This work was supported by the Natural Sciences and Engineering Research Council of Canada (Grant No. RGPIN-2020-06101). We would also like to acknowledge the support from Mitacs Globalink Research Internship for providing the internship opportunity to A.V.

Informed Consent Statement: Not applicable.

Data Availability Statement: Not applicable.

Conflicts of Interest: The authors declare no conflict of interest.

Appendix A. Ensemble Averaging

The surge front is transient and moves with a celerity that is approximated by the Method of Characteristics (MOC). The ensembles, therefore, have a space lag, x_{lag}, moving with surge wave celerity, c. The ensemble-averaged results were obtained by using 100 ensembles between $t = 4$ s and 6 s, when the turbulence at the wave front was fully developed. To capture this transient nature, a 4 m rectangular domain spanning from $x_1 = 35$ m to $x_2 = 39$ m was selected at $t = 4.00$ s. The domain boundaries in the x-direction moved with the surge wave celerity of c, estimated from the MOC. In cases where the shifted boundaries did not overlap with the grid alignment, a weighted algorithm was

applied. The weight factors were determined based on the distance to the two adjacent grid points. This is demonstrated in Figure A1 for $t = 4.05$ s and $Fr_s = 2.13$, where the celerity is $c = 2.9835$ m/s.

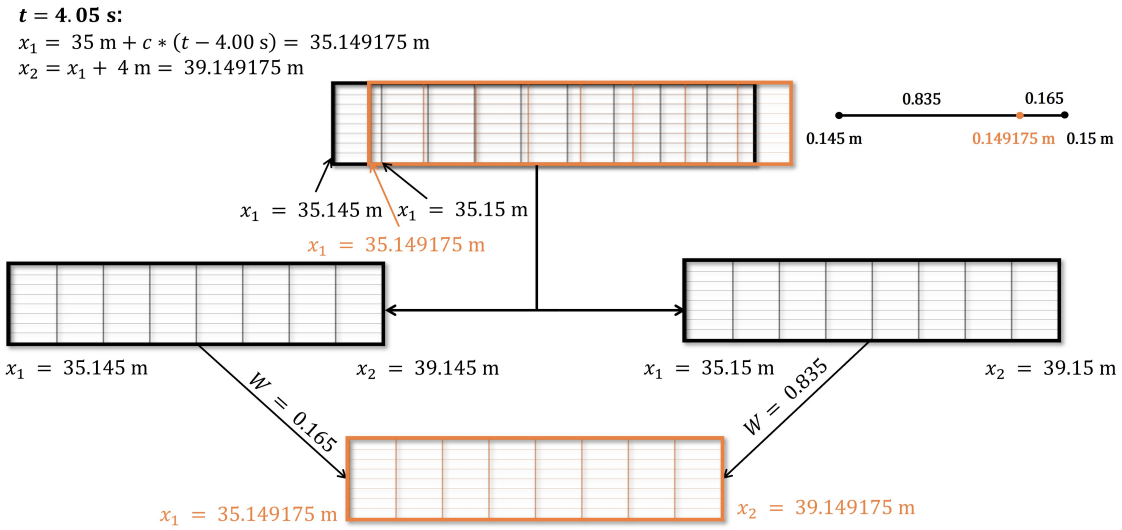

Figure A1. Illustration of the weighted algorithm at $t = 4.05$ s for $c = 2.9835$ m/s and a uniform grid of $\Delta x = 0.005$ m. The boundaries of the ensemble box are located at $x_1 = 35$ m and $x_2 = 39$ m at $t = 4.00$ s. The weighted factors, W, were calculated based on the vicinity of the shifted domain to the nearest grid point.

References

1. Xie, P.; Chu, V.H. The forces of tsunami waves on a vertical wall and on a structure of finite width. *Coast. Eng.* **2019**, *149*, 65–80. [CrossRef]
2. Chanson, H. *Hydraulics of Open Channel Flow*; Elsevier: Amsterdam, The Netherlands, 2004.
3. Gilmore, F.; Plesset, M.; Crossley, H., Jr.; The analogy between hydraulic jumps in liquids and shock waves in gases. *J. Appl. Phys.* **1950**, *21*, 243–249. [CrossRef]
4. Karimpour, S.; Chu, V.H. High-order interpolation schemes for shear instability simulations. *Int. J. Numer. Methods Heat Fluid Flow* **2015**, *25*, 1340–1360. [CrossRef]
5. Karimpour, S.; Chu, V.H. The role of waves on mixing in shallow waters. *Can. J. Civ. Eng.* **2019**, *46*, 134–147. [CrossRef]
6. Leng, X.; Chanson, H. Upstream propagation of surges and bores: Free-surface observations. *Coast. Eng. J.* **2017**, *59*, 1750003. [CrossRef]
7. Li, Y.; Chanson, H. Sediment motion beneath surges and bores. In Proceedings of the Daniel Bung, Blake Tullis, 7th IAHR International Symposium on Hydraulic Structures, Aachen, Germany, 15–18 May 2018. [CrossRef]
8. Chanson, H.; Tan, K.K. Particle dispersion under tidal bores: Application to sediments and fish eggs. In Proceedings of the 7th International Conference on Multiphase Flow ICMF 2010, Tampa, FL, USA, 30 May–4 June 2010.
9. Takahashi, M.; Ohtsu, I. Effects of inflows on air entrainment in hydraulic jumps below a gate. *J. Hydraul. Res.* **2017**, *55*, 259–268. [CrossRef]
10. Chanson, H. Free-surface aeration in dam break waves: An experimental study. In Proceedings of the International Conference on Hydraulics of Dams and River Structures, Tehran, Iran, 26–28 April 2004.
11. Zheng, F.; Li, Y.; Xuan, G.; Li, Z.; Zhu, L. Characteristics of positive surges in a rectangular channel. *Water* **2018**, *10*, 1473. [CrossRef]
12. Ting, F.C. Large-scale turbulence under a solitary wave. *Coast. Eng.* **2006**, *53*, 441–462. [CrossRef]
13. Kimmoun, O.; Branger, H. A particle image velocimetry investigation on laboratory surf-zone breaking waves over a sloping beach. *J. Fluid Mech.* **2007**, *588*, 353–397. [CrossRef]
14. Watanabe, Y.; Saeki, H.; Hosking, R.J. Three-dimensional vortex structures under breaking waves. *J. Fluid Mech.* **2005**, *545*, 291–328. [CrossRef]
15. Lubin, P.; Glockner, S. Numerical simulations of three-dimensional plunging breaking waves: generation and evolution of aerated vortex filaments. *J. Fluid Mech.* **2015**, *767*, 364–393. [CrossRef]
16. Leng, X.; Simon, B.; Khezri, N.; Lubin, P.; Chanson, H. CFD modeling of tidal bores: Development and validation challenges. *Coast. Eng. J.* **2018**, *60*, 423–436. [CrossRef]

17. Munters, W.; Meneveau, C.; Meyers, J. Shifted periodic boundary conditions for simulations of wall-bounded turbulent flows. *Phys. Fluids* **2016**, *28*, 025112. [CrossRef]
18. Pope, S.B. *Turbulent Flows*; Cambridge University Press: Cambridge, UK, 2001.
19. Chanson, H.; Lubin, P.; Glockner, S. *Unsteady Turbulence in a Shock: Physical and Numerical Modelling in Tidal Bores and Hydraulic Jumps*; Nova Science Publishers: Hauppauge, NY, USA, 2012.
20. Yoshizawa, A.; Horiuti, K. A statistically-derived subgrid-scale kinetic energy model for the large-eddy simulation of turbulent flows. *J. Phys. Soc. Jpn.* **1985**, *54*, 2834–2839. [CrossRef]
21. Almeland, S. Implementation of an air-entrainment model in interFoam. In *Proceedings of CFD with OpenSource Software*; Nilsson, H., Ed.; Chalmers University of Technology: Göteborg, Sweden, 2018.
22. Cifani, P.; Michalek, W.; Priems, G.; Kuerten, J.G.; van der Geld, C.; Geurts, B.J. A comparison between the surface compression method and an interface reconstruction method for the VOF approach. *Comput. Fluids* **2016**, *136*, 421–435. [CrossRef]
23. Greenshields, C.J. *OpenFOAM User Guide*; OpenFOAM Found, Ltd.: London, England, 2015; Volume 3, p. 47.
24. Chen, L.; Zang, J.; Hillis, A.J.; Morgan, G.C.; Plummer, A.R. Numerical investigation of wave–structure interaction using OpenFOAM. *Ocean Eng.* **2014**, *88*, 91–109. [CrossRef]
25. Kim, J.; Moin, P.; Moser, R. Turbulence statistics in fully developed channel flow at low Reynolds number. *J. Fluid Mech.* **1987**, *177*, 133–166. [CrossRef]
26. Karimpour, S.; Wang, T.; Chu, V.H. The exchanges between the mainstream in an open channel and a recirculating flow on its side at large Froude numbers. *J. Fluid Mech.* **2021**, *920*, A8. [CrossRef]
27. Matheou, G.; Chung, D. Large-eddy simulation of stratified turbulence. Part II: Application of the stretched-vortex model to the atmospheric boundary layer. *J. Atmos. Sci.* **2014**, *71*, 4439–4460. [CrossRef]
28. Koch, C.; Chanson, H. Turbulence measurements in positive surges and bores. *J. Hydraul. Res.* **2009**, *47*, 29–40. [CrossRef]
29. Leng, X.; Chanson, H. Coupling between free-surface fluctuations, velocity fluctuations and turbulent Reynolds stresses during the upstream propagation of positive surges, bores and compression waves. *Environ. Fluid Mech.* **2016**, *16*, 695–719. [CrossRef]
30. Rajaratnam, N. *Advances in Hydroscience*; Academic Press: New York, NY, USA, 1967; Volume 4.
31. Wüthrich, D.; Shi, R.; Chanson, H. Physical study of the 3-dimensional characteristics and free-surface properties of a breaking roller in bores and surges. *Exp. Therm. Fluid Sci.* **2020**, *112*, 109980.
32. Chanson, H. Two-phase flow characteristics of an unsteady dam break wave flow. In Proceedings of the 30th IAHR Biennial Congress, Thessaloniki, Greece, 24 August–29 2003.
33. Wang, H.; Chanson, H. Air entrainment and turbulent fluctuations in hydraulic jumps. *Urban Water J.* **2015**, *12*, 502–518. [CrossRef]
34. Lu, S.; Willmarth, W. Measurements of the structure of the Reynolds stress in a turbulent boundary layer. *J. Fluid Mech.* **1973**, *60*, 481–511. [CrossRef]
35. Rajagopalan, S.; Antonia, R. Use of a quadrant analysis technique to identify coherent structures in a turbulent boundary layer. *Phys. Fluids* **1982**, *25*, 949–956. [CrossRef]
36. Hunt, J.C.R.; Wray, A.A.; Wray, P. Eddies, Stream, and Convergence Zones in Turbulent Flows. Studying Turbulence Using Numerical Simulation Databases, 2. Available online: https://ntrs.nasa.gov/citations/19890015184 (accessed on 7 June 2021).